10C survey of radio sources at 15.7 GHz - II. First results

Davies, M.L.; Franzen, T.M.O.; Waldram, E.M.; Grainge, K.J.B.; Hobson, M.P.; Hurley-Walker, N.; … ; Zwart, J.T.L.

Version:	Not Applicable (or Unknown)
License:	
Downloaded from:	https://hdl.handle.net/1887/59592

10C survey of radio sources at 15.7 GHz – II. First results[★]

AMI Consortium: Matthew L. Davies,[1]† Thomas M. O. Franzen,[1]†
Elizabeth M. Waldram,[1] Keith J. B. Grainge,[1,2] Michael P. Hobson,[1]
Natasha Hurley-Walker,[1] Anthony Lasenby,[1,2] Malak Olamaie,[1] Guy G. Pooley,[1]
Julia M. Riley,[1] Carmen Rodríguez-Gonzálvez,[1] Richard D. E. Saunders,[1,2]
Anna M. M. Scaife,[3] Michel P. Schammel,[1] Paul F. Scott,[1] Timothy W. Shimwell,[1]
David J. Titterington[1] and Jonathan T. L. Zwart[4]

[1]*Astrophysics Group, Cavendish Laboratory, 19 J. J. Thomson Avenue, Cambridge CB3 0HE*
[2]*Kavli Institute for Cosmology Cambridge, Madingley Road, Cambridge CB3 0HA*
[3]*Dublin Institute for Advanced Studies, 31 Fitzwilliam Place, Dublin 2, Ireland*
[4]*Columbia Astrophysics Laboratory, Columbia University, 550 West 120th Street, New York, NY 10027, USA*

ABSTRACT

In a previous paper (Paper I), the observational, mapping and source-extraction techniques used for the Tenth Cambridge (10C) Survey of Radio Sources were described. Here, the first results from the survey, carried out using the Arcminute Microkelvin Imager Large Array (LA) at an observing frequency of 15.7 GHz, are presented. The survey fields cover an area of $\approx 27\,\mathrm{deg}^2$ to a flux-density completeness of 1 mJy. Results for some deeper areas, covering $\approx 12\,\mathrm{deg}^2$, wholly contained within the total areas and complete to 0.5 mJy, are also presented. The completeness for both areas is estimated to be at least 93 per cent. The 10C survey is the deepest radio survey of any significant extent ($\gtrsim 0.2\,\mathrm{deg}^2$) above 1.4 GHz.

The 10C source catalogue contains 1897 entries and is available online. The source catalogue has been combined with that of the Ninth Cambridge Survey to calculate the 15.7-GHz source counts. A broken power law is found to provide a good parametrization of the differential count between 0.5 mJy and 1 Jy. The measured source count has been compared with that predicted by de Zotti et al. – the model is found to display good agreement with the data at the highest flux densities. However, over the entire flux-density range of the measured count (0.5 mJy to 1 Jy), the model is found to underpredict the integrated count by ≈ 30 per cent.

Entries from the source catalogue have been matched with those contained in the catalogues of the NRAO VLA Sky Survey and the Faint Images of the Radio Sky at Twenty-cm survey (both of which have observing frequencies of 1.4 GHz). This matching provides evidence for a shift in the typical 1.4-GHz spectral index to 15.7-GHz spectral index of the 15.7-GHz-selected source population with decreasing flux density towards sub-mJy levels – the spectra tend to become less steep.

Automated methods for detecting extended sources, developed in Paper I, have been applied to the data; ≈ 5 per cent of the sources are found to be extended relative to the LA-synthesized beam of ≈ 30 arcsec. Investigations using higher resolution data showed that most of the genuinely extended sources at 15.7 GHz are classical doubles, although some nearby galaxies and twin-jet sources were also identified.

Key words: catalogues – surveys – radio continuum: galaxies – radio continuum: general.

1 INTRODUCTION

1.1 Background

The Ninth Cambridge (9C) Survey of Radio Sources (Waldram et al. 2003, 2010), carried out using the Ryle Telescope (RT) at an

---

observing frequency of 15.2 GHz, was a milestone in the exploration of the high-radio-frequency sky, as the first survey of significant extent and depth at such a high radio frequency. Since the publication of the first 9C paper, extensive survey work has been carried out using the Australia Telescope Compact Array at 20 GHz (ATCA; Ricci et al. 2004; Sadler et al. 2006; Massardi et al. 2008, 2011; Murphy et al. 2010). The two surveys are complementary, with the 9C survey probing deeper flux-density levels (down to 5.5 mJy) and the ATCA surveys covering shallower and wider areas (most recently, the whole southern sky).

It is well known that high-frequency radio surveys are highly time-consuming. The scaling of interferometer primary-beam areas with frequency ($\propto \nu^{-2}$) and the typical synchrotron spectra of radio sources ($\propto \nu^{-0.7}$) conspire so that the time required to carry out a survey of equivalent depth and sky coverage, using a telescope of a fixed aperture diameter, scales as $\nu^{3.4}$. Things are somewhat better if it is assumed that the available bandwidth scales linearly with frequency. However, the fact that the noise temperatures of the available front-end, low-noise amplifiers used in interferometers tend to increase with frequency must also be taken into account.

For these reasons, relatively little survey work has been undertaken at high radio frequencies and the knowledge of the source population remains poor. Nevertheless, the familiarity with the properties of this population is important for the interpretation of the results from observations of the cosmic microwave background (CMB), such as those made by *Planck* (Tauber et al. 2010). At mm wavelengths, foreground radio sources are the dominant source of the contamination of small-scale CMB anisotropies (de Zotti et al. 1999). Waldram et al. (2003, 2010) have demonstrated that the extrapolation of the flux densities of sources at low frequencies cannot be relied upon to predict their high-frequency properties, which emphasizes the value of survey work at the frequencies of interest ($\gtrsim 10$ GHz) for CMB work.

Samples of bright sources selected at high radio frequencies have significant proportions with flat or rising spectra (see e.g. Taylor et al. 2001; AMI Consortium: Davies et al. 2009). These sources are mainly believed to be blazars with synchrotron self-absorbed spectra; the self-absorbed components of such sources are often highly variable (see e.g. AMI Consortium: Franzen et al. 2009).

High-frequency-selected samples also include appreciable numbers of sources with convex spectra, peaking at GHz frequencies (see e.g. Bolton et al. 2004). Some of these GHz peaked spectrum (GPS) sources (see O'Dea 1998, for a review) are believed to be associated with young objects, which later expand into powerful radio sources, though many are dominated by the emission from a strongly beamed self-absorbed component (Bolton et al. 2006). Surveys such as the 9C survey provide flux-density-limited samples, which are useful for gaining further understanding of the evolution of such objects.

1.2 This work

Since the 9C survey was carried out, the RT has been transformed, by the installation of new front-end receivers and back-end electronics (including a new correlator), into the Arcminute Microkelvin Imager (AMI) Large Array (LA) (see AMI Consortium: Zwart et al. 2008, for a detailed description of the telescope). The LA is a radio synthesis telescope located ≈ 19 m above the sea level near Cambridge. It is used to observe at a centre frequency of 15.7 GHz and has a usable bandwidth of 4.5 GHz. At this frequency, the telescope has a full width at half-maximum (FWHM) primary beam of ≈ 5.5 arcmin and a resolution of ≈ 30 arcsec.

The LA has been used to carry out the Tenth Cambridge (10C) Survey of Radio Sources. As part of this survey, the improved flux sensitivity of the LA, compared with the RT, has been used to explore the 15-GHz-band sky to sub-mJy levels. In a previous paper (AMI Consortium: Franzen et al. 2011, hereinafter Paper I), detailed technical information regarding the survey strategy, mapping and source-extraction techniques for the 10C survey was provided. In this paper, the first results from 10 fields, including the 15.7-GHz source count, are presented. Throughout this paper, any equatorial coordinates use equinox J2000 and spectral indices are defined using the convention that $S \propto \nu^{-\alpha}$.

2 THE 10C SOURCE CATALOGUE

The techniques used for observing, mapping and source extraction are fully described in Paper I. The fields, the positions of which are given in Section 3, were surveyed using a 'rastering' technique, with observations being carried out between 2008 August and 2010 June. Each field was observed using a set of telescope pointing directions spaced at 4.0 arcmin intervals and lying on a 2D hexagonally gridded lattice, projected on to the plane of the sky. A raster map that combines the individual CLEANed maps belonging to each of the pointing directions was produced for each field; the raster map for one of the survey fields is shown in Fig. 1. In addition, a noise map that shows how the noise varies across the raster map was created for each field; these noise maps are used in identifying sources, as described in Paper I.

Information about the sources was extracted from the raster maps, using a combination of in-house software and tasks belonging to the AIPS,[1] for the inclusion in the 10C source catalogue. Source finding was carried out using a flux-density threshold of 4.62σ; the reason for this slightly unusual choice is explained in Sections 2.1 and 2.2.

In Section 3, areas within each of the survey fields, bounded by lines of constant right ascension (RA) and declination (Dec.), complete to flux densities of 1.0 and 0.5 mJy, are defined. A short section of the catalogue is shown in Table 1. The methods used to extract various parameters are fully described in Paper I; the final column indicates which of the areas (see Section 3) each of the sources lies within. The complete source list, which contains 1897 entries, is available online (see Supporting Information), along with an explanatory readme file. This information can also be found on the survey website (http://www.mrao.cam.ac.uk/surveys/10C), where it is also planned to make the FITS maps for each of the survey fields publicly available, once further 10C observations have been completed.

Individual positional error estimates have not been assigned to each source. The positional errors in both RA and Dec. for a source detected at the 5σ level, in any of the survey fields, are estimated to be 3–4 arcsec; this range reflects the fact that the synthesized beam is slightly elliptical and has dimensions which vary with field declination. The assessment of the source positional accuracy was made using simulations in which point sources were inserted into the map of one of the survey fields; the extracted source positions were compared with the nominal values.

The results of the simulation were found to agree well with the positional errors that would be expected from theory, taking into account Gaussian thermal noise. Higher resolution follow-up observations are required to assess the positional accuracy for the brighter sources. Only the highest-flux-density source in the 10C

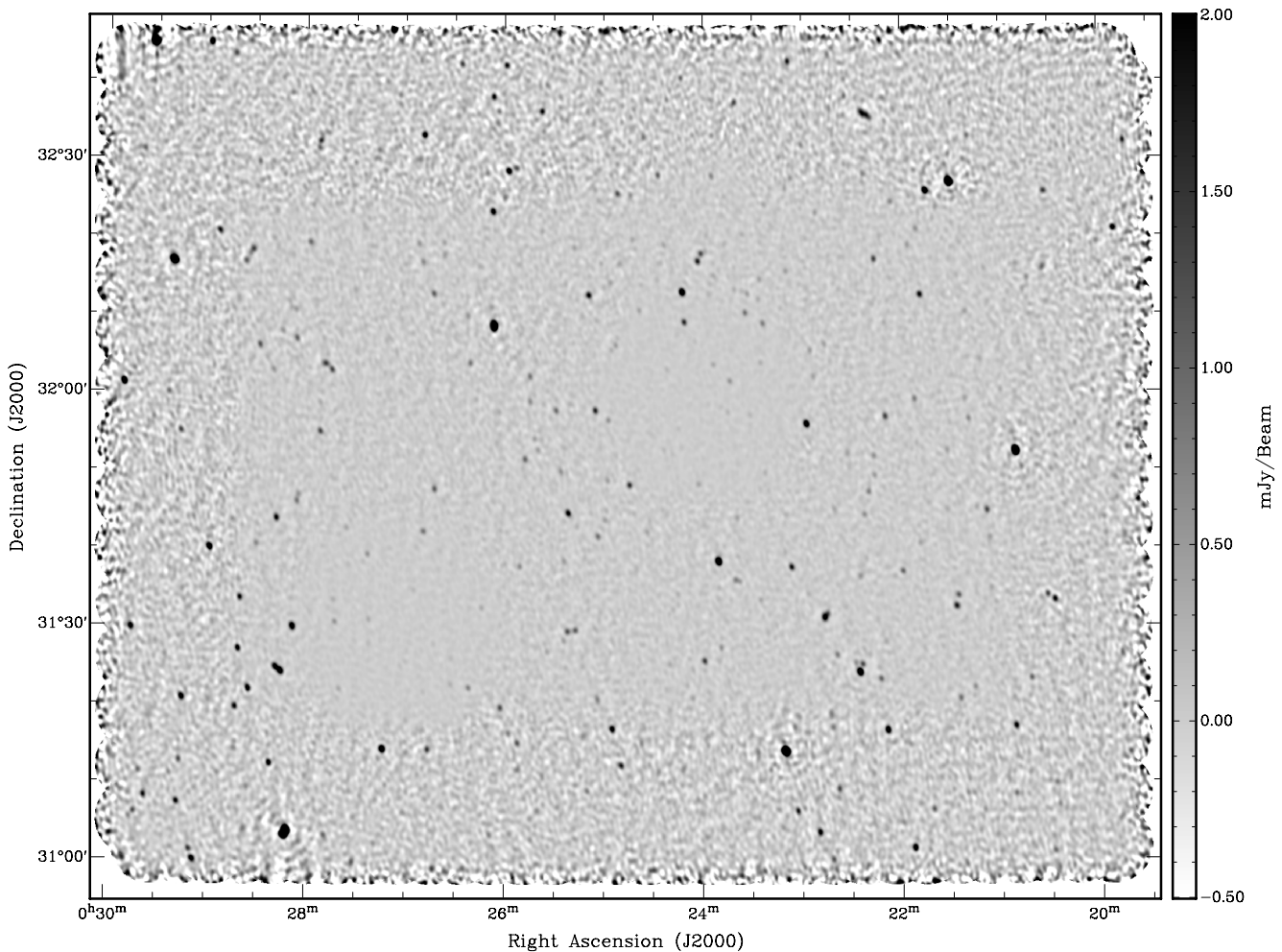[1] Astronomical Image Processing System – http://www.aips.nrao.edu

Figure 1. The raster map of one of the 10C survey fields (J0024+3152). The map was produced by combining approximately 1000 individual constituent maps, weighted according to their rms noise; the individual maps were CLEANed before being combined. The area of lower noise at the centre of the raster map is clearly visible.

survey catalogue has a counterpart in the catalogue of the Jodrell Bank-VLA Astrometric Survey (Patnaik et al. 1992; Browne et al. 1998; Wilkinson et al. 1998). The measured positions of this source agree within 3.5 arcsec.

There were some problems with the analysis and mapping of the 10C survey data that required some adaptations to the source-finding procedure described in Paper I. These adaptations are described in the remainder of this section.

2.1 Checking the flux-density scale

As a check of the raster maps' flux-density scale, ≈50 of the brightest sources detected in the maps were selected for pointed follow-up observations, carried out during 2010 June and August using the LA. To avoid complicating the analysis, only sources that showed no evidence of extension in the raster maps were selected. The data from these observations were mapped using the same CLEANing scheme as used for the raster maps, but phase self-calibration was also applied.

Fig. 2 shows the peak flux densities for each of the sources measured using the raster and (self-calibrated) pointed maps. The figure indicates that the flux densities of the sources measured from the raster maps are systematically low compared with those from the self-calibrated pointed observations. However, because the pointed

follow-up observations were carried out about 2 yr after the commencement of the raster observations, it is important to consider the effect of source variability on this result.

Fig. 2 indicates that the pointed flux density of one source is almost twice its raster flux density; this difference is almost certainly attributable to genuine flux-density variability. Having said this, the number of genuinely variable sources within the sample is likely to be small. The sources selected for pointed follow-up have flux densities ranging between approximately 10 and 40 mJy. Results from Waldram et al. (2010) indicate that 15-GHz-selected samples containing sources with flux densities in this range are likely to be dominated by steep-spectrum sources, which do not ordinarily display significant variability.

Nevertheless, the median percentage difference has been used to quantify the discrepancy between the pointed and raster flux densities because it is less sensitive to genuine source variability than the mean, the value of which could be strongly affected by a small number of highly-variable sources within the sample. The median percentage difference between the pointed and raster flux densities was calculated to be 8.2 per cent with an uncertainty in this value of ≈2 per cent.

Since a number of the 10C survey fields overlap with areas mapped as part of the 9C survey, as an additional check, the flux

Table 1. Samples from the 10C source catalogue, which is available in full online with an explanatory readme file (see Supporting Information). [This information can also be found on the survey website (www.mrao.cam.ac.uk/surveys/10C), where it is also planned to make the FITS maps for each of the survey fields publicly available, once further 10C observations have been completed.] The extraction procedures for the various parameters are fully described in Paper I. The columns are the source name; the group name, which indicates overlapping sources (the group is named after the source with the highest peak flux density in the group and the number of objects in the group is given in brackets); RA, α_{pk} (J2000), and Dec., δ_{pk} (J2000), of the source peak; the peak flux density, S_{pk}, and its uncertainty, δS_{pk}; RA, α_{in}, and Dec., δ_{in}, of the source centroid (J2000; relevant for extended sources); the integrated flux density, S_{in}, and its uncertainty, δS_{in}; the critical value, e_{crit}, of the major-axis, above which the source is defined as extended, having deconvolved the telescope's point-source response from the fitted 2D Gaussian; the lengths, e_{maj} and e_{min}, of the major-axis and minor-axis and position angle, e_θ, of the source after the deconvolution – the e_{min} and e_θ columns are left blank for sources classified as point like; the source type, t – point like (P) or extended (E); a flag, '*', indicating that the error from the approximation of the point-source response is significant and, consequently, the results from the Gaussian fitting ought to be treated with caution; and the region of the survey in which the source falls – deep (D), shallow (S) or neither (N). Note that the parameters from the Gaussian fitting are omitted if the fitting did not converge.

| Source name	Group name	α_{pk}	δ_{pk}	S_{pk} (mJy)	δS_{pk} (mJy)	α_{in}	δ_{in}	S_{in} (mJy)	δS_{in} (mJy)	e_{crit} (arcsec)	e_{maj} (arcsec)	e_{min} (arcsec)	e_θ (°)	t	Flag	Region
10C J002129+322700		00:21:29.8	+32:27:00	24.69	1.34	00:21:29.9	+32:27:01	23.27	1.28	25.0	13.5			P	*	S
10C J002215+314923		00:22:15.8	+31:49:23	0.51	0.07	00:22:15.8	+31:49:25	0.40	0.09	43.2	0.0			P		D
10C J002215+321707		00:22:15.8	+32:17:07	1.55	0.10	00:22:15.8	+32:17:07	1.47	0.13	25.0	9.5			P		D
10C J002216+315153		00:22:16.2	+31:51:53	0.64	0.07	00:22:16.2	+31:51:52	0.56	0.10	39.1	0.0			P		D
10C J002219+314717		00:22:19.3	+31:47:17	0.83	0.08	00:22:19.3	+31:47:19	0.76	0.11	34.2	11.9			P		D
10C J002220+323537	10C J002222+323549(2)	00:22:20.0	+32:35:37	2.15	0.20	00:22:19.4	+32:35:31	3.51	0.44	32.5	58.2	0.0	49.7	E		S
10C J002221+314422		00:22:21.9	+31:44:22	0.67	0.07	00:22:22.0	+31:44:21	0.61	0.10	36.3	0.0			P		D
10C J002222+322803		00:22:22.1	+32:28:03	0.77	0.15	00:22:22.0	+32:28:04	0.77	0.24	52.3	9.4			P		S
10C J002222+323549	10C J002222+323549(2)	00:22:22.3	+32:35:49	2.40	0.21	00:22:22.8	+32:35:51	3.17	0.40	30.9	44.9	0.0	41.7	E		S
10C J002223+312509	10C J002224+312409(3)	00:22:23.3	+31:25:09	1.46	0.10	00:22:23.4	+31:25:10	1.36	0.12	25.0	5.3			P		D
10C J002224+313627		00:22:24.4	+31:36:27	0.62	0.06	00:22:24.4	+31:36:29	0.74	0.11	35.5	31.9			P		D
10C J002224+312409	10C J002224+312409(3)	00:22:24.9	+31:24:09	6.86	0.37	00:22:24.9	+31:24:10	7.14	0.40	25.0	9.1			P		D
10C J002227+312520	10C J002224+312409(3)	00:22:27.4	+31:25:20	0.66	0.07	00:22:27.3	+31:25:19	0.59	0.10	36.5	4.3			P		D
10C J002232+315213		00:22:32.1	+31:52:13	0.44	0.07	00:22:32.1	+31:52:15	0.56	0.13	47.8	33.7			P		D
10C J002233+323802		00:22:33.4	+32:38:02	1.04	0.18	00:22:33.6	+32:38:02	0.97	0.27	47.9	7.6			P		S
10C J002237+310910		00:22:37.7	+31:09:10	1.50	0.17	00:22:37.6	+31:09:11	1.51	0.27	40.7	17.2			P		S
10C J002238+312622		00:22:38.6	+31:26:22	0.88	0.08	00:22:38.7	+31:26:23	0.84	0.11	31.0	7.1			P		D
10C J002240+314503		00:22:40.1	+31:45:03	0.41	0.07	00:22:40.0	+31:45:00	0.51	0.13	47.9	44.9			P		S
10C J002241+310007		00:22:41.3	+31:00:07	1.34	0.20	00:22:41.3	+31:00:06	1.33	0.33	49.7	16.7			P		S
10C J002241+311704		00:22:41.3	+31:17:04	0.89	0.14	00:22:41.2	+31:17:04	0.92	0.23	49.2	15.9			P		S
10C J002242+311844		00:22:42.3	+31:18:44	0.84	0.11	00:22:42.2	+31:18:43	1.28	0.24	40.9	43.7	0.0	0.2	E		S
10C J002246+313113		00:22:46.0	+31:31:13	3.33	0.19	00:22:45.8	+31:31:16	5.22	0.31	25.0	42.9	9.0	145.3	E		D
10C J002246+320614		00:22:46.1	+32:06:14	0.47	0.07	00:22:46.2	+32:06:15	0.40	0.10	43.8	11.6			P		D
10C J002249+310336		00:22:49.3	+31:03:36	2.82	0.21	00:22:49.4	+31:03:37	2.96	0.30	29.4	10.9			P		S
10C J002251+322305		00:22:51.3	+32:23:05	0.50	0.08	00:22:51.3	+32:23:06	0.39	0.10	45.7	0.0			P		D
10C J002252+320204		00:22:52.7	+32:02:04	0.46	0.05	00:22:52.7	+32:02:06	0.52	0.09	37.1	27.6			P		D
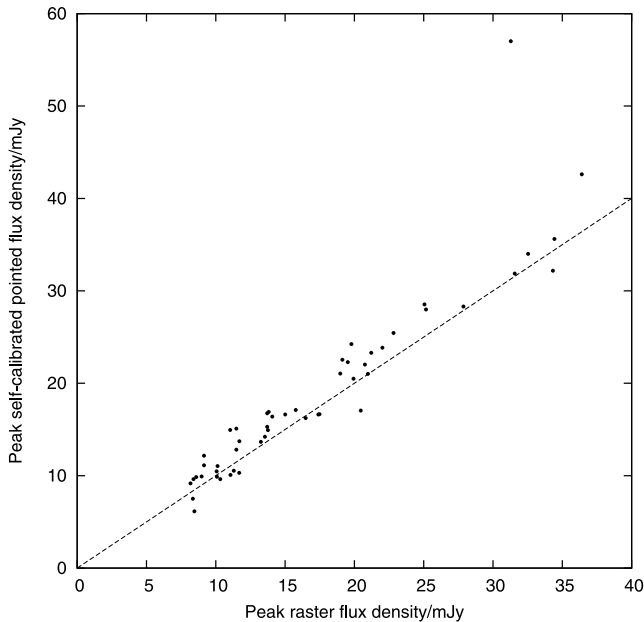
Figure 2. The peak flux densities of ≈50 sources as measured from the raster maps and from maps created using self-calibrated data from pointed follow-up observations. Points lying on the line represent sources having identical flux densities when measured using the raster and pointed maps.

densities measured from the pointed observations were compared with the values measured from pointed 9C observations. Having corrected the phase errors in the 10C pointed observations using self-calibration, there was found to be good agreement between the 9C and 10C pointed values with a median percentage difference of <1 per cent – the median is again used for the same reason as given above. It is noted that, owing to the small difference in the observing frequencies and the typical spectra of radio sources, the 10C flux densities might be expected to be slightly lower than the 9C values – this was, in fact, the case.

Data from a large number of observations, carried out during a range of weather conditions, were combined to create the raster maps; whereas the data used to produce the pointed maps were collected during single, short observations during relatively good (dry) observing conditions. As a result, the weather conditions during the pointed observations may not be typical of those during the raster observations. However, in practice, data collected during periods of poor weather are either omitted entirely or significantly downweighted with respect to data collected during good weather conditions.

A modulated noise signal, injected at the front end of each antenna, was monitored throughout the raster observations. The data were then weighted, on a sample-by-sample basis, according to the value of the 'rain gauge' – that is the ratio of the power of the modulated noise signal to the total power input to the correlator (which is kept constant) to that obtained in cool, dry, clear weather conditions. In addition, data for which the rain gauge was less than 50 per cent (this is rather a conservative criterion) were omitted. This is because the amplitude correction applied to the data becomes unreliable during heavy rain, as no attempt to account for atmospheric absorption is made in applying this correction.

Atmospheric-related phase effects are not thought to make any significant contribution to the phase errors present in the data. During LA observations, a phase-calibrator source is observed

for 1 min at 10 min intervals. Even using the telescope's longest (110-m) baseline, the measured phase varies only slowly on time-scales much longer than 10 min. If the measured phase for a calibrator source does change by more than 30° between successive visits to the source, the affected data are automatically omitted during the data-reduction stage; however, such a large phase difference between successive calibrator visits is observed only very rarely. Similarly, any data for which the estimated error in the measured phase of the calibrator is >15° are also omitted automatically.

The discrepancy between the flux densities measured using the phase-self-calibrated pointed observations and the raster observations is instead attributed to phase errors in AMI data resulting from the uneven spacings of the time-delays in the telescope's lag correlator. Holler et al. (2007) explain this problem in detail and propose a solution. In practice, however, further work is required to analyse the data from the correlator correctly.

2.2 Correcting the sources' flux densities for phase errors

Unfortunately, the great majority of the sources in the 10C raster maps are detected with an insufficient signal-to-noise ratio (S/N) to allow self-calibration to be successfully applied to the data. Therefore, a correction to the source flux densities based on the difference between the flux densities measured from the raster maps and the self-calibrated pointed maps is applied; as a final step in the source-finding procedure, all source flux densities are multiplied by 1.082 before their inclusion in the 10C catalogue.

The uncertainties in the flux densities are increased to take account of this scaling and the uncertainty in the correction factor (≈2 per cent), which is in any case small compared with the estimated LA calibration uncertainty of 5 per cent. As in Paper I, the uncertainty in an uncorrected peak flux density, S, is taken to be $\sqrt{\sigma_n^2 + (0.05S)^2}$, where σ_n is the thermal noise at the source position, estimated from the noise map. The uncertainty in the corrected value is therefore

$$1.082S\sqrt{\frac{\sigma_n^2 + (0.05S)^2}{S^2} + 0.02^2}. \qquad (1)$$

Initially, it was intended to carry out source finding at 5σ; since, assuming Gaussian statistics for the map noise, such a scheme would result in a highly reliable catalogue with ≈0.1 false detections. Further, the completeness of such a catalogue would have been very high ($\gtrsim$94 per cent) at 0.5 and 1 mJy in the deep and shallow regions, respectively. However, owing to the effect of phase errors, a source of $S = 1$ mJy falling within the shallow area of the survey, which ought to be detected at $\geq 5\sigma$, will only be detected at $\geq 5\sigma/1.082 = 4.62\sigma$.

Therefore, in order to achieve the desired high levels of completeness at 0.5 and 1 mJy, it was decided to carry out the source finding at 4.62σ. The catalogue completeness is fully discussed in Section 4. The slight relaxation in the source-finding criterion is likely to have only a small adverse effect on the reliability of the catalogue. Assuming Gaussian statistics for the map noise, and given the number of synthesized beam areas in the survey maps, it is estimated that about one source in the final catalogue will be a false positive.

2.3 Excluding areas around bright sources

The 10C raster maps often display an increased level of noise around bright ($\gtrsim$15 mJy) sources. This is attributable to amplitude, phase and deconvolution errors in the data. The elevated noise level close

to bright sources is generally not fully reflected by the noise maps, because the noise is highly non-Gaussian in these regions. Therefore, such detections close to sources of $S > 15$ mJy were automatically excluded from the final source catalogue. In addition, detections close to a number of fainter sources (the faintest being ≈ 9 mJy) were also excluded manually from the final catalogue after inspecting the maps.

Empirically, the area of the elevated noise around each bright source (the 'exclusion zone'), from which the source detections were rejected, was found to be well represented by a circle, centred on the source position, of radius

$$r_e = 12 \left(\frac{S_{pk}/\text{mJy}}{250} \right)^{1/2} \text{arcmin,} \qquad (2)$$

where S_{pk} is the peak flux density of the source. Table 2 shows the centre coordinates and radii of the exclusion zones applied to the survey data.

The dynamic range of the LA – that is the ratio of a source's peak flux density to the flux density of the brightest artefact in a map close to the source – is ≈ 50:1. The brightest source detected in the 10C survey is ≈ 270 mJy. A conservative approach, which also serves to simplify the completeness areas for the construction of the source count, has been taken by assuming that sources with $S \geq 9$ mJy can be detected anywhere in the total areas. In contrast, any putative source with a peak flux density less than this value that falls within the exclusion zone of a bright source is not included in the final 10C source catalogue. Thus, the area used for calculating the source counts for sources with $S < 9$ mJy does not include the exclusion zones around bright sources. The total area excluded from around bright sources is 0.6 deg^2.

3 SURVEY FIELDS

The 10C survey fields are centred at J0024+3152, J0259+2610, J0734+5432, J0824+6931, J0939+3115, J1046+5904, J1052+5730, J1524+4321, J1543+4420 and J1733+4148. Fig. 3 shows the positions of these fields, which were chosen to be widely spread in RA and away from the Galactic plane. For each field, areas complete to 1.0 and 0.5 mJy (apart from the exclusion zones) have been defined by selecting those areas in which the noise, σ_n, estimated using the relevant noise map is $0.1 \leq \sigma_n < 0.2$ mJy and $\sigma_n < 0.1$ mJy, respectively. Over a large portion of the areas, the estimated noise is significantly lower than the upper bounds and therefore the completeness is close to 100 per cent for both regions at their nominal completeness levels.

The areas complete to 0.5 mJy are entirely contained within the areas complete to 1.0 mJy and are referred to as the 'deep' regions. Areas of higher noise, complete to 1.0 mJy, but excluding the deep regions, are referred to as the 'shallow' areas. Fig. 4 shows the deep and shallow regions for one of the fields. The survey catalogue includes a flag for each source, indicating whether it falls in the deep (D) or shallow (S) areas. Sources that fall outside these regions altogether (i.e. in areas of higher noise towards the edges of the raster maps) are indicated by 'N'. For a source with evidence of extension, the flag is based on the source's centroid position; otherwise, the peak position is used. The 'total' areas are those areas complete to 1 mJy but not excluding the deep regions – in other words, the combined deep and shallow areas. The lines of RA and Dec. bounding the total and deep areas, for each of the fields, are given in Tables 3 and 4, respectively.

Table 2. The centre positions of the exclusion zones around bright sources and their radii.

RA	Dec.	Radius (arcmin)
00:20:50.4	+31:52:29	3.39
00:21:29.8	+32:26:60	3.63
00:23:09.9	+31:14:01	4.26
00:26:06.2	+32:08:33	2.83
00:28:10.7	+31:03:46	3.85
00:29:20.4	+32:16:55	3.17
00:29:33.1	+32:44:58	4.45
02:59:55.1	+26:27:26	2.31
03:01:05.5	+25:47:16	2.92
03:01:37.3	+25:41:54	3.04
07:31:17.4	+53:38:58	4.25
07:36:52.9	+54:29:17	2.70
08:18:16.1	+69:16:53	4.06
08:23:02.5	+69:14:20	2.94
09:35:59.5	+31:27:27	3.17
09:36:36.9	+32:03:35	3.31
09:37:06.2	+32:06:58	5.41
09:41:03.2	+31:26:14	3.30
09:41:46.2	+31:55:03	3.05
09:42:08.8	+32:06:42	3.48
10:47:19.3	+58:21:14	4.93
10:49:40.0	+58:35:31	3.35
10:50:07.1	+56:53:37	3.38
10:50:54.0	+58:32:33	3.50
10:51:41.4	+59:13:08	3.80
10:52:25.4	+57:55:08	3.46
10:52:54.5	+59:22:18	3.56
10:54:26.9	+57:36:48	3.69
15:20:41.6	+44:13:18	3.43
15:21:49.4	+43:36:37	12.51
15:27:51.8	+43:52:05	2.85
15:28:19.8	+42:33:35	4.01
15:40:33.5	+44:34:01	3.32
15:41:10.0	+44:56:34	4.58
15:42:23.1	+43:59:15	3.81
15:46:04.5	+44:49:14	3.02
17:25:34.5	+41:53:03	4.33
17:27:49.3	+42:21:40	4.45
17:29:01.9	+41:40:04	2.68
17:30:41.6	+41:02:58	6.14
17:31:23.7	+41:01:38	3.01
17:37:59.6	+41:54:51	5.00
17:38:35.4	+42:21:43	3.08
17:40:08.9	+41:36:09	6.31
17:40:17.2	+42:14:30	2.93
17:40:52.1	+42:34:47	5.79

4 COMPLETENESS

4.1 Simulations

Simulations were carried out to investigate the completeness of the survey. A number of realizations were used (12 for the deep areas and 13 for the shallow) in which 250 equal-flux-density, simulated point sources were inserted into the raster map of J0024+3152. The flux density of the simulated sources was different for each of the realizations. The positions of the simulated sources were chosen randomly but were not altered between realizations; to avoid the simulated sources affecting each other, it was insisted that no simulated source could lie within 2 arcmin of any other. Sources were not inserted in the exclusion zones around bright sources,
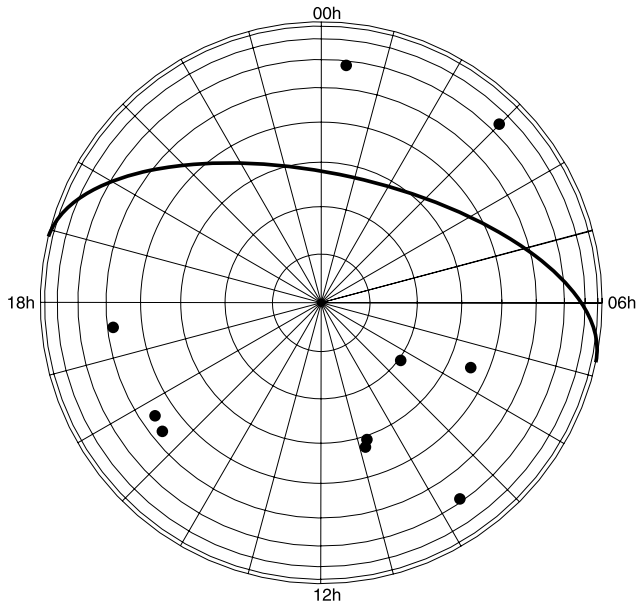
Figure 3. The positions of the 10C survey fields, shown using an equatorial-plane projection with the North Pole at the centre. The declination circles are at intervals of 10° and the Galactic plane is indicated by the thick black line.
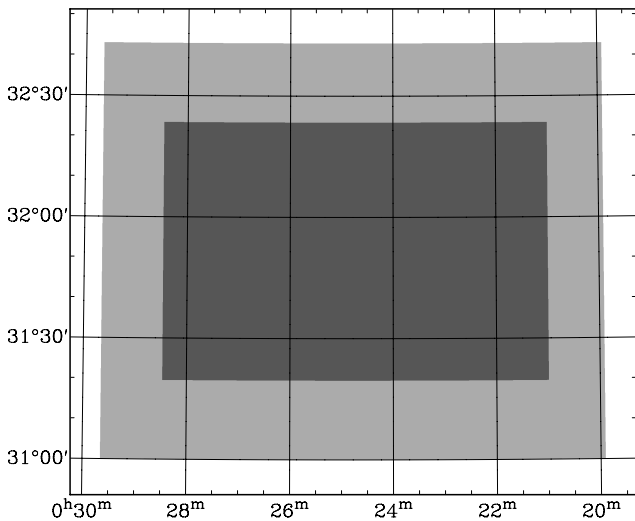

Figure 4. The shallow (lighter shading) and deep areas belonging to J0024+5432.

since, as explained above, the completeness limit is expected to be much higher for these areas compared with the remainder of the maps. In order to investigate the completeness as a function of flux density, the flux density of the sources was changed between realizations.

For each realization, the ordinary source-finding procedures were applied to the map and the proportion of simulated sources that were recovered was calculated for the shallow and deep areas. Three of the simulated sources were found to lie too close to real sources to be detected separately. In these cases, the simulated source was considered to be detected if the recovered source position was closer to the simulated rather than the real source position.

Fig. 5 shows the proportion of sources detected for each of the realizations compared with the expected detection rate, which is calculated for a particular region of the map as follows. For a specific

source flux density, the probability of detection can be calculated at the position of each pixel by taking account of the value of the noise map at that position and by using Gaussian statistics. The probability of detection over the whole region is straightforwardly calculated by averaging over pixels.

The plots show that, in general, there is good agreement between the predicted completeness curves and the results of the simulation. However, for the fainter sources, the detection rate is slightly higher than predicted, whilst the converse is true for the brighter sources. Source confusion is likely to be responsible for these results. A number of the highest flux-density simulated sources, that would otherwise have been detected, were not recovered owing to their proximity to real, bright sources. This effect prevented the completeness from reaching 100 per cent as quickly as predicted. At fainter flux densities, however, the opposite effect, whereby a source is boosted in flux density owing to its proximity to a real, fainter source, so that it is unexpectedly detected, becomes important.

The peak flux densities of sources detected with low S/Ns are typically biased slightly high, because the peak position tends to be coincident with a positive noise fluctuation. This is an additional factor serving to boost the detection rate at low S/Ns. The presence of this effect was confirmed by extracting the flux densities of the sources at the precise positions with which they were simulated; the values were found to be systematically low compared with the extracted *peak* flux densities and were found to reflect better the simulated flux densities.

4.2 Using the noise maps to estimate the completeness

Having established by simulation that, assuming Gaussian statistics for the noise, the noise maps can be used to provide reasonable estimates of the survey completeness, the noise maps from all the fields were used to estimate the completeness of the 10C survey. The probability of a source with the true flux density $\hat{S}$ being included in the survey catalogue when located on a pixel with a corresponding noise-map value of σ_n was taken, according to Gaussian statistics, to be

$$P(\hat{S} \geq 4.62\sigma_n) = \int_{4.62\sigma_n}^{\infty} \frac{1}{\sqrt{2\pi\sigma_n^2}} \exp -\frac{\left(x - \hat{S}/1.082\right)^2}{2\sigma_n^2} \, dx. \quad (3)$$

In carrying out this calculation, the fact that sources are detected with flux densities lower than their true values has been taken into account by including the factor of 1/1.082.

Knowing the actual distribution of noise-map pixel values, equation (3) can be used to estimate the completeness, as a function of flux density, for the shallow and deep regions of the survey; Fig. 6 shows these estimates for both areas. For the shallow regions, the catalogue is estimated to be ≈94 per cent complete by 1 mJy and 99 per cent complete by ≈1.16 mJy. For the deep areas, the catalogue is estimated to be ≈93 per cent complete by 0.5 mJy and 99 per cent complete by ≈0.61 mJy.

5 SOURCE COUNTS

The 15.7-GHz differential source counts have been calculated by binning the sources from the final catalogue according to their peak flux densities, except for those that display evidence of being extended relative to the telescope-synthesized beam (this is the case for 5.5 per cent of sources), for which integrated flux densities were used.

The binned differential-source-count data are given in Table 5. For the highest flux-density bin, data from the entirety of the total areas have been used. The bins for sources with flux densities between
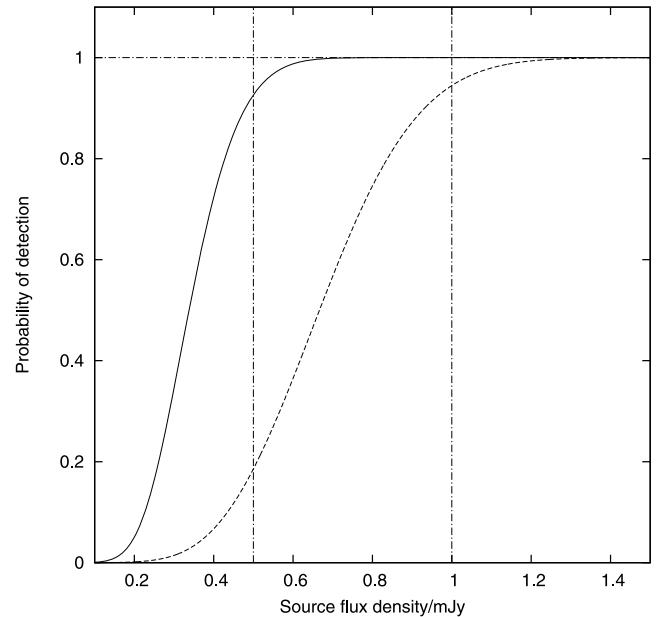
Table 3. The areas complete to 1 mJy.

Field	RA range	Dec. range	Area (deg^2)
J0024+3152	00:19:54.2 to 00:29:38.3	+31:00:04 to +32:43:05	3.56
J0259+2610	02:56:43.6 to 03:02:32.8	+25:19:17 to +27:02:17	2.24
J0734+5432	07:30:02.8 to 07:38:50.7	+53:41:42 to +55:23:07	2.16
J0824+6931	08:17:08.6 to 08:31:23.8	+68:41:04 to +70:22:41	2.11
J0939+3115	09:36:22.1 to 09:42:25.9	+30:24:22 to +32:06:18	2.20
J1046+5904	10:39:25.5 to 10:52:31.2	+58:13:12 to +59:55:07	2.86
J1052+5730	10:47:36.8 to 10:57:21.3	+56:48:56 to +58:10:22	1.78
J1524+4321	15:20:10.7 to 15:29:24.6	+42:30:20 to +44:11:21	2.83
J1543+4420	15:38:30.5 to 15:47:46.6	+43:28:43 to +45:11:13	2.83
J1733+4148	17:25:37.0 to 17:41:01.3	+40:57:34 to +42:40:06	4.90

Table 4. The areas complete to 0.5 mJy. Note that there are three deep regions associated with J0259+2610.

Field	RA range	Dec. range	Area (deg^2)
J0024+3152	00:20:59.1 to 00:28:27.1	+31:19:38 to +32:23:29	1.69
J0259+2610	02:57:50.5 to 03:01:24.1	+25:38:31 to +26:43:51	0.87
	02:56:50.2 to 02:57:50.5	+25:53:05 to +26:28:22	0.13
	03:01:24.1 to 03:02:31.4	+25:53:05 to +26:28:22	0.15
J0734+5432	07:31:47.0 to 07:37:06.6	+54:00:59 to +55:04:59	0.82
J0824+6931	08:19:21.5 to 08:29:26.1	+68:57:47 to +70:07:19	1.02
J0939+3115	09:37:32.8 to 09:41:15.9	+30:42:52 to +31:47:13	0.85
J1046+5904	10:41:30.0 to 10:50:24.5	+58:32:47 to +59:35:08	1.19
J1052+5730	10:49:57.7 to 10:55:32.7	+57:08:03 to +57:51:28	0.54
J1524+4321	15:21:32.3 to 15:27:57.3	+42:50:56 to +43:52:21	1.19
J1543+4420	15:39:51.6 to 15:46:21.3	+43:49:49 to +44:50:48	1.18
J1733+4148	17:26:44.0 to 17:39:49.8	+41:17:01 to +42:19:40	2.54
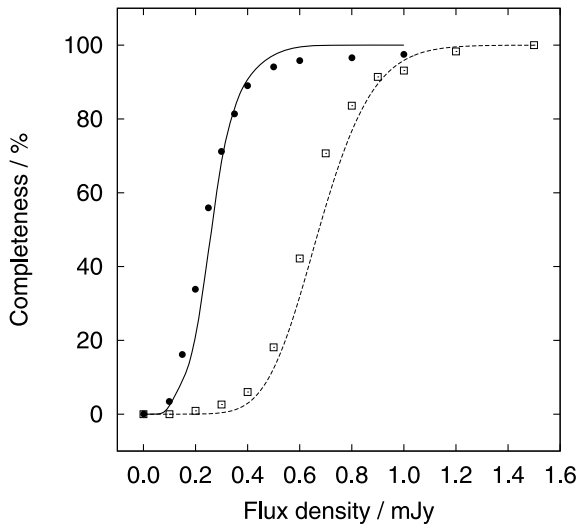
Figure 5. Results of a simulation to investigate the completeness of the survey. The filled circles show the proportion of the simulated sources recovered as a function of flux density within the deep ($\sigma_n \leq 0.1$ mJy) area of J0024+3152. The solid line shows the completeness predicted based on the noise-map pixel values, assuming Gaussian statistics for the noise. The open squares and dashed line show the results for the shallow ($0.1 < \sigma_n \leq 0.2$ mJy) area.

Figure 6. The estimated probability of detection for the shallow (dashed line) and deep (solid line) areas of all survey fields. The dot–dashed horizontal line indicates a probability of 1. The dot–dashed vertical lines indicate the 0.5- and 1.0-mJy nominal completeness limits for the deep and shallow areas, respectively.

1 and 9 mJy include sources from the total regions but exclude the areas around bright sources given in Table 2. The bins for sources with flux densities between 0.5 and 1 mJy include sources from the deep regions (again excluding areas around bright sources). The source count is not calculated for $S > 25$ mJy, since it is biased low

in this flux-density range; using 9C data, several of the fields were selected to contain as few sources with $S > 25$ mJy as possible.

At 0.5 mJy, the completeness limit of the deep areas, the survey is limited by thermal rather than confusion noise. Above this

Table 5. Data for the 10C source count.

Bin start S (mJy)	Bin end S (mJy)	Number of sources	Area (deg^2)
9.000	25.000	46	27.46
5.500	9.000	51	26.86
2.900	5.500	142	26.86
2.050	2.900	135	26.86
1.500	2.050	148	26.86
1.250	1.500	113	26.86
1.000	1.250	160	26.86
0.900	1.000	36	11.96
0.775	0.900	56	11.96
0.680	0.775	51	11.96
0.600	0.680	64	11.96
0.540	0.600	61	11.96
0.500	0.540	46	11.96

flux-density level, it is estimated that there are typically 170 LA-synthesized beam areas per source.

The effect of the calibration errors of ≈ 5 per cent is negligible, serving to boost the number of sources in each bin by $\ll 1$ per cent (owing to the sign of the slope of the source count). However, the bias (Eddington 1913) due to the thermal noise will play a more important role for the bins at the faintest flux-density levels. Given the slope of the counts and the noise properties of the deep region, the number of sources in the faintest flux-density bin is expected to be boosted by ≈ 7 per cent. However, this effect is almost exactly balanced by the small degree of incompleteness that affects these faintest flux-density bins. Consequently, no corrections for the effect of Eddington bias or incompleteness have been applied.

The 10C differential source count is shown in Fig. 7. As in all subsequent plots showing source counts, Poisson errors, on the number of sources in each bin, are indicated for each of the points and the bars parallel to the flux-density axis represent the bin widths, not error bars.

Figure 7. The 10C differential source count. Poisson errors, on the number of sources in each bin, are indicated for each of the points. The bars parallel to the flux-density axis represent the bin widths, not error bars. The fitted broken-power-law count is indicated by the solid line.
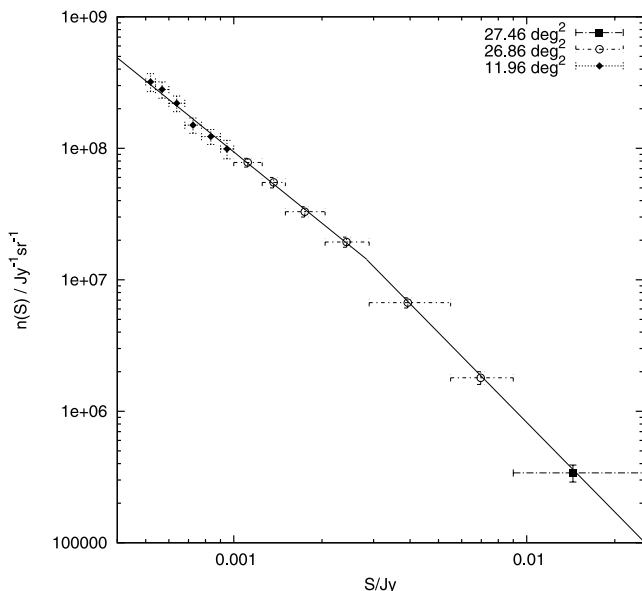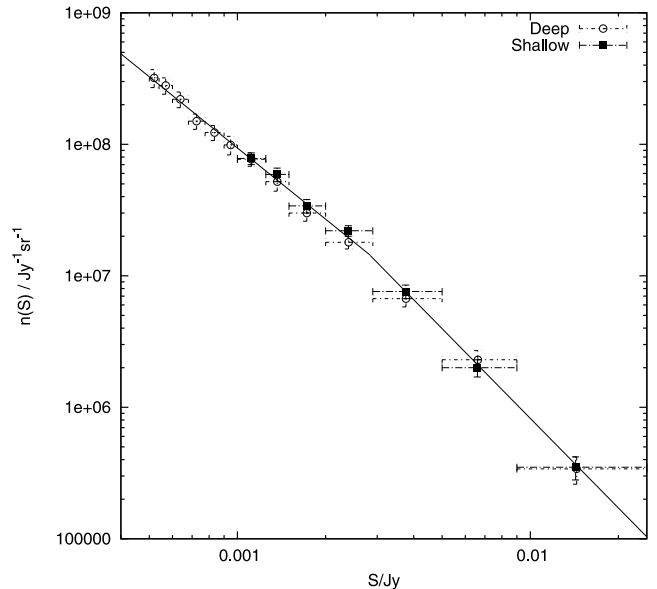

Figure 8. Differential source counts from the shallow and deep regions of the 10C survey. The fitted 10C source count is indicated by the solid line.

An attempt was made to fit a single power law to the data. However, such a model did not appear to fit the data well. Consequently, a broken power law has been fitted to the data. A method was used whereby the sum of the squared differences between the measured and predicted areas under the curve, over all bins, was minimized. In carrying out the minimization, the points were weighted according to their respective Poisson errors. The positions of the points in the S direction within the bins have been plotted, in Fig. 7, on the basis of the fitted exponents to reflect the 'centre of gravity' of each bin. The fitted differential source count is

$$n(S) \equiv \frac{dN}{dS} \approx \begin{cases} 24 \left(\frac{S}{\text{Jy}} \right)^{-2.27} \text{Jy}^{-1}\,\text{sr}^{-1} & \text{for } 2.8 \leq S \leq 25 \text{ mJy} \\ 376 \left(\frac{S}{\text{Jy}} \right)^{-1.80} \text{Jy}^{-1}\,\text{sr}^{-1} & \text{for } 0.5 \leq S < 2.8 \text{ mJy.} \end{cases}$$

Tests were carried out to check that the broken-power-law model does indeed provide an improved fit to the data, compared with the single-power-law model. An F-test indicated that the null hypothesis – that the data are more likely to have been drawn from the simpler model – can be rejected at >99.9 per cent confidence. A comparison of the models using Akaike's information criterion was similarly emphatic, indicating that the broken-power-law model is ≈ 1000 times more likely to be correct than the simpler model.

In order to check the self-consistency of the source count, the data were used to construct separate counts for the shallow and deep regions. Fig. 8 shows the counts from the two regions overlaid. The deep counts are derived from an area amounting to $11.96 \, \text{deg}^2$ (except for the highest flux-density bin, which contains data from $12.19 \, \text{deg}^2$). The shallow counts use data from $14.90 \, \text{deg}^2$ ($15.27 \, \text{deg}^2$ for the highest flux-density point). The plot shows good agreement, within the uncertainties, between the counts derived from the two regions over the common flux-density range.

5.1 Adding in data from the 9C survey

It is possible to extend the 10C source count to higher flux densities by the inclusion of data from the 9C survey. It is also possible

to improve the source count statistics between 5.5 and 25 mJy by including 9C data, since the 9C survey contains regions that are complete over this flux-density range. There is a small difference in the observing frequencies of the 9C (15.2 GHz) and 10C surveys (15.7 GHz). Therefore, in combining the data sets, the source flux densities from the 9C survey catalogue have been corrected to take into account this difference. The correction was made by assuming a typical spectral index between 15.2 and 15.7 GHz that varies as a function of source flux density.

The assumed flux-density-dependent spectral index is indicated in Fig. 9. The correction was calculated by fitting a logarithmic function to the points in the plot. For each of the three lowest flux-density points (indicated by the filled squares), the median flux density versus the median value of the 1.4- to 15.2-GHz spectral index, $\alpha_{1.4}^{15.2}$, of sources, with flux densities in the relevant ranges, detected as part of the 9C survey (see table 9 of Waldram et al. 2010) has been plotted. For the highest flux-density point (indicated by the filled triangle), the median flux density versus median value of α_{16}^{33}, measured by AMI Consortium: Davies et al. (2009), for sources belonging to a flux-density-limited source sample (López-Caniego et al. 2007) from the 3-yr *Wilkinson Microwave Anisotropy Probe* (*WMAP*) data has been plotted. The number of sources belonging to the samples represented by these points ranges between 84 and 381.

For both the 9C and *WMAP* samples, it has simply been assumed that the spectral indices can be extended over the small additional frequency ranges to 15.7 GHz (from 15.2 GHz in the case of the 9C samples and from 16 GHz for the *WMAP* sample). The approach followed is admittedly not perfect, particularly since the sample for
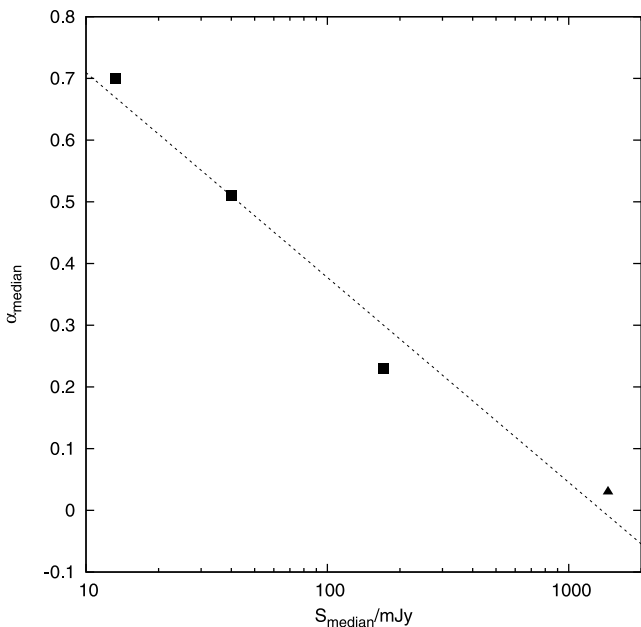
the highest flux-density point was selected at 33 GHz. Nevertheless, because the difference in observing frequencies between the surveys is very small, the corrections are similarly small (at most a few per cent) and the method is considered acceptable.

Fig. 10 shows the combined 9C and 10C differential source count. Data from areas of the 9C survey presented in Waldram et al. (2003) and Waldram et al. (2010) have been used in constructing the count. The data used for each bin are shown in Table 6. For the intermediate flux-density ranges, for which there are data from both surveys, some of the 9C survey data were excluded. This was to avoid double counting the areas that were surveyed as part of both the 9C and 10C surveys.

Using the same method as described above, a broken power law was fitted to the binned differential count. As previously, a broken power law was found to be a significantly better fit to the data than a single power law. Again, an F-test indicated that the null hypothesis – that the data are more likely to have been drawn from the simpler model – can be rejected at >99.9 per cent confidence. The best-fitting broken-power-law parametrization of the source count is

$$n(S) \equiv \frac{dN}{dS} \approx \begin{cases} 48 \left(\frac{S}{Jy} \right)^{-2.13} \ Jy^{-1} \ sr^{-1} \ \text{for } 2.2 \ mJy \leq S \leq 1 \ Jy \\ 340 \left(\frac{S}{Jy} \right)^{-1.81} \ Jy^{-1} \ sr^{-1} \ \text{for } 0.5 \leq S < 2.2 \ mJy. \end{cases}$$

This fitted count is found to give a good fit to the data, with a reduced chi-squared value of 0.75. The probability of obtaining a reduced chi-squared value greater than 0.75 by chance, given the number (20) of degrees of freedom, is 78 per cent. The fit is indicated in Fig. 10.

5.2 Comparison with the de Zotti model

In Fig. 11, the combined 9C and 10C source count is compared with the latest version of the 15-GHz source-count model by de Zotti et al. (2005), extracted from their website[2] on 2011 March 1; for completeness, the model counts, over the relevant flux-density range, are provided in Appendix A. No attempt has been made to correct for the small frequency difference between the measured and model source counts but this is likely to make little difference to the overall conclusions.

The model count is in good agreement with the measured count at the high-flux-density end. However, the shape of the plotted model count is somewhat different from that of the measured count; so that, with decreasing flux density, the model first overpredicts and then, below $\approx$5 mJy, underpredicts the measured count.

The total number of sources per steradian with flux densities between 0.5 mJy and 1 Jy, predicted by the model, was calculated by integrating the model differential source count between these limiting flux densities. Since the predicted counts are given at a number of discrete flux densities (see Table A1), the integration was carried out piecewise by approximating the model count as a power law between successive pairs of points.

The number of sources per unit area predicted by the model was found to be only 70 per cent of the measured value. Because the differential count is largest at the low-flux-density end, the underprediction of the count at the lowest flux densities dominates over the overprediction at slightly higher flux densities, explaining the 30 per cent deficit over the entire range.

Figure 9. The filled squares represent the median 1.4- to 15.2-GHz spectral indices for complete 15.2-GHz-selected source samples from the 9C survey. The filled triangle represents the median 16- to 33-GHz spectral index for a complete 33-GHz-selected sample from the *WMAP* 3-yr data. The dashed line indicates the assumed typical spectral index, as a function of flux density, used to make corrections to the flux densities of individual 9C sources, to account for the small difference in the observing frequencies of the 9C and 10C surveys. This allowed the 10C source count to be extended to flux densities >25 mJy by the inclusion of 9C data. The typical spectral index was calculated by fitting a logarithmic function to the data points.

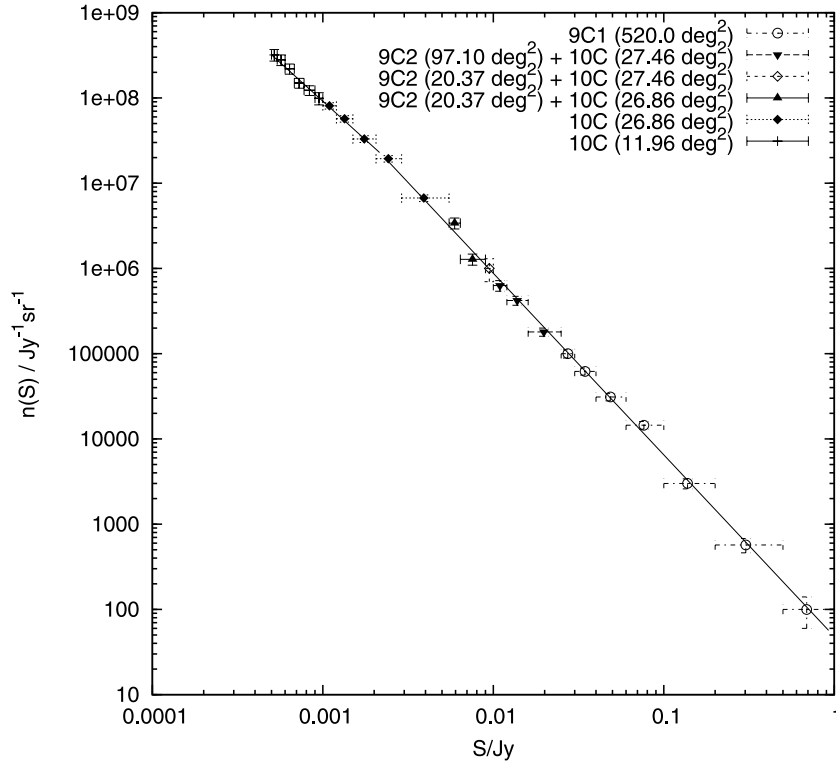[2] http://web.oapd.inaf.it/rstools/srccnt/srccnt_tables

Figure 10. The combined 9C and 10C 15.7-GHz differential source count. Different symbols are used to distinguish between the areas that were used to derive the count for the various flux-density bins: '9C1' indicates areas presented in Waldram et al. (2003); '9C2' refers to areas presented in Waldram et al. (2010); and '10C' is used to designate areas presented in this paper. The fitted count is indicated by the solid line.

Table 6. Data for the combined 9C and 10C source counts.

| Bin start S (mJy)	Bin end S (mJy)	Number of sources	Area (deg²)
500.000	1000.000	8	520.00
200.000	500.000	27	520.00
100.000	200.000	47	520.00
60.000	100.000	92	520.00
40.000	60.000	97	520.00
30.000	40.000	99	520.00
25.000	30.000	79	520.00
16.000	25.000	62	124.60
12.000	16.000	64	124.60
10.000	12.000	48	124.60
9.000	10.000	15	47.83
6.400	9.000	48	47.23
5.500	6.400	44	47.23
2.900	5.500	142	26.86
2.050	2.900	135	26.86
1.500	2.050	148	26.86
1.200	1.500	140	26.86
1.000	1.200	133	26.86
0.900	1.000	36	11.96
0.775	0.900	56	11.96
0.680	0.775	51	11.96
0.600	0.680	64	11.96
0.540	0.600	61	11.96
0.500	0.540	46	11.96
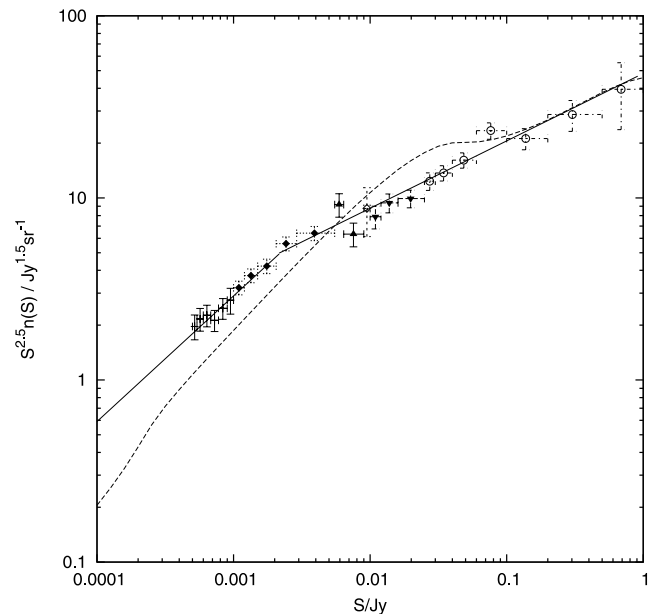
Figure 11. The normalized ($S^{2.5} \frac{dN}{dS}$) combined 9C and 10C differential source count. The symbols indicating the areas from which the counts were derived are identical to those in Fig. 10. The fitted broken-power-law parametrization is indicated by the solid line. The dashed line indicates the prediction of the latest version of the de Zotti et al. (2005) model.

6 MATCHING WITH 1.4-GHZ SURVEYS

The complete and unbiased sample of sources from the deep areas of the survey (i.e. those sources with flux densities between 0.5 and 25 mJy in these areas) was matched with entries from the 1.4-GHz catalogues of the Faint Images of the Radio Sky at Twenty-cm (FIRST; Becker, White & Helfand 1995) survey and the NRAO VLA Sky Survey (NVSS; Condon et al. 1998). The sample comprises ≈650 sources in total. There are NVSS data for all the 10C survey fields; however, some of the 10C survey fields are not covered or are only partially covered by the FIRST survey.

The NVSS, which has a resolution of 45 arcsec (slightly lower than that of the 10C survey), has a completeness of 50 per cent at ≈2.5 mJy and 99 per cent at ≈3.4 mJy. The FIRST survey has higher resolution of 5 arcsec and is complete to 1 mJy. Owing to the significant difference in resolution between the 10C and FIRST surveys, the flux densities of any FIRST sources lying within one LA-synthesized beam of a 10C source were summed for comparison with the 10C flux density.

Some results from the matching with the NVSS and FIRST catalogues are shown in Tables 7 and 8, respectively. In both cases, the sample has been divided into various 15.7-GHz flux-density bins and the percentage of sources with flux densities falling in each bin without a corresponding match in the relevant low-frequency catalogue is indicated. A limiting 1.4- to 15.7-GHz spectral index, α_{lim}, based on the completeness limit of the relevant low-frequency catalogues (3.4 mJy for the NVSS and 1.0 mJy for the FIRST survey), is also indicated for each bin. Any source with a spectral index greater than this limiting value ought to be detected in the low-frequency catalogue.

In addition, the percentage of sources with $\alpha > 0.5$ and $\alpha > 0.81$ is given for each bin. For the matching to the NVSS catalogue, for all but the three highest flux-density bins, the percentages of sources with $\alpha > 0.5$ ought to be regarded as lower limits. This is because the values of α_{lim}, for the lower flux-density bins, are >0.5. The choice of the second value of 0.81 avoids this problem, since

for all flux-density bins and for matching to both low-frequency catalogues, all sources with $\alpha > 0.81$ should be matched.

It is noted that the percentages of sources with $\alpha > 0.5$ and $\alpha > 0.81$ from matching to the FIRST survey are systematically lower than those from matching to the NVSS. This is most likely due to the fact that the extended emission detected as part of the NVSS is resolved as part of the FIRST survey.

An interesting effect, whereby the source population shifts towards a flatter-spectrum population with decreasing flux density, is observed in the data. This is most clearly seen in the matching to the NVSS from the change in the fraction of sources with $\alpha > 0.81$. As mentioned previously, the fraction of sources with $\alpha > 0.5$ represents a lower limit for a number of bins and so the evolution in this fraction cannot readily be interpreted as evidence for a change in the population. In the matching to the FIRST survey, the effect is best demonstrated by the change in the fraction of sources with $\alpha > 0.5$. Owing to the fact that FIRST coverage is not available for all the 10C fields, the statistics for the fractions of sources with $\alpha > 0.81$ are poorer compared with those for the matching with the NVSS. Also, the interpretation of the results is complicated by the mismatch in resolution noted above.

By matching sources detected as part of the 9C survey to the NVSS catalogue, Waldram et al. (2010) observed a shift in the 15-GHz-band source population from being dominated by a flat-spectrum to being dominated by steep-spectrum sources with decreasing flux density between ≈100 and ≈10 mJy – this effect is illustrated by Fig. 9. A similar effect has been observed by Massardi et al. (2011) by matching entries from their 20-GHz source catalogue to low-frequency catalogues. Their large sample size allows them to trace the spectral evolution of the source population in detail between 40 mJy and 1 Jy. The median value of $\alpha_{1.4}^{20}$ is found to become rapidly larger with decreasing flux density below ≈80 mJy (E. Sadler, private communication).

The 10C data suggest that, at fainter flux densities, this trend is reversed with a move back towards a flatter spectrum population. A shift towards a flatter spectrum population has been observed in

Table 7. Some statistics from matching with the NVSS source catalogue. The numbers and percentages of sources with $\alpha > 0.5$ for the lowest four flux-density bins are lower limits.

Bin start S (mJy)	Bin end S (mJy)	Total	Matched	Unmatched	α_{lim}	Percentage unmatched	$\alpha > 0.5$	Percentage $\alpha > 0.5$	$\alpha > 0.81$	Percentage $\alpha > 0.81$
5.0	25.0	55	54	1	−0.15	2	38	69	27	49
2.5	5.0	65	62	3	0.14	5	47	72	30	46
1.5	2.5	99	87	12	0.35	12	64	74	45	46
1.0	1.5	114	76	38	0.52	33	>67	>59	29	25
0.8	1.0	79	50	29	0.61	37	>42	>53	22	28
0.6	0.8	125	60	65	0.73	52	>59	>47	26	21
0.5	0.6	107	43	64	0.81	60	>43	>40	19	18

Table 8. Some statistics from matching with the FIRST source catalogue.

Bin start S (mJy)	Bin end S (mJy)	Total	Matched	Unmatched	α_{lim}	Percentage unmatched	$\alpha > 0.5$	Percentage $\alpha > 0.5$	$\alpha > 0.81$	Percentage $\alpha > 0.81$
5.0	25.0	36	36	0	−0.67	0	17	47	8	22
2.5	5.0	46	44	2	−0.38	4	23	50	7	15
1.5	2.5	56	50	6	−0.17	11	30	54	8	14
1.0	1.5	67	50	17	0.00	25	24	36	10	15
0.8	1.0	50	41	9	0.09	18	18	36	5	10
0.6	0.8	88	56	32	0.21	36	35	40	15	17
0.5	0.6	68	32	36	0.29	53	18	27	7	10

sub-mJy data from low-frequency surveys (see e.g. Prandoni et al. 2006, and references therein).

7 EXTENDED SOURCES

Using the methods described in Paper I, 4.8 per cent of the 10C sources are classified as extended and 5.9 per cent as overlapping (the categories are mutually exclusive). Some of the 'extended' sources might be classified as such owing to the source confusion or effects arising from noise. Similarly, chance juxtapositions of sources are likely to result in sources with no genuine association being classified as overlapping. Consequently, simulations in which simulated point sources were inserted, at randomly selected positions, into the 10C survey fields were carried out in an attempt to provide an estimate of the fraction of 10C sources that are genuinely extended relative to the LA-synthesized beam.

In total, ≈ 1600 simulated point sources were added into the 10C data in the *uv*-plane. The sources were simulated with flux densities drawn randomly from the measured source count. As for the simulation to assess the survey completeness, no simulated source was allowed to lie within 2 arcmin of any other. The standard mapping and source extraction procedures, described in Paper I, were applied to the data. Of the simulated point sources that were detected, 1.4 ± 0.5 per cent were classified as extended and 2.2 ± 0.4 per cent were categorized as overlapping, where the uncertainties have been estimated from the scatter in the results between the different survey fields.

The results from the simulation suggest that $\approx 100 \times (4.8 - 1.4)/4.8 \approx 71$ per cent of the sources classified as such are genuinely extended and that $\approx 100 \times (5.9 - 2.2)/5.9 \approx 63$ per cent of overlapping sources are actually a component of a larger object. In the great majority of cases, overlapping sources are found to have just two components. Therefore, if the two categories are taken together – that is, sources consisting of a single component that is extended relative to the telescope-synthesized beam and extended sources consisting of several overlapping components – the fraction of 10C sources that are genuinely extended relative to the LA-synthesized beam of ≈ 30 arcsec is estimated as $(5.9 - 2.2)/2 + (4.8 - 1.4) \approx 5$ per cent (the factor of 1/2 results from the assumption that the overlapping sources consist of two components). This result assumes no clustering of sources on small ($\lesssim 1$ arcmin) angular scales. It is noted that a similar fraction (≈ 6 per cent) of extended sources was measured from 9C data by Waldram et al. (2003), who carried out the classification on the basis of the manual inspection of 9C contour maps.

Contour plots of all the sources identified by the automated source-extraction procedures as extended or overlapping were inspected by eye. Sources thought most likely to be genuinely extended from their morphologies (e.g. overlapping sources with similar peak flux densities) were identified. 10C contour plots of 39 such sources were compared with contour plots from the NVSS and, where available, from the FIRST survey. In addition, the NASA Extragalactic Data base[3] (NED) was searched for objects detected within ≈ 2 arcmin of each of the extended 10C sources. The NED reports entries from catalogues belonging to a number of low-frequency radio surveys, in addition to entries from the catalogues of optical, infrared and X-ray surveys.

From these investigations, 29 of the 39 sources were found to be genuinely extended and two artefacts of source confusion. In

[3] http://nedwww.ipac.caltech.edu

eight cases, it still remains unclear whether the sources were genuinely extended. Most of the genuinely extended sources were found to be classical doubles but three are nearby galaxies and four are twin-jet/tailed sources. One of the twin-jet sources has $z = 0.267$ and another has $z = 0.391$; the respective centroid positions of these sources are 15:41:05.0, +43:27:00 and 10:44:56.7, +59:25:38. Some results for one source of particular interest are provided below.

7.1 8C 0821+695

It was noted, whilst manually inspecting the contour plots of two sources flagged as extended, that these sources were the lobes of a 'linear triple', a broad-emission-line radio galaxy or radio-loud quasar (see Fig. 12). The central component and outer lobes span an angular distance of 6.6 arcmin and appear as three separate sources in the 10C catalogue, since no linking emission is detected using the 10C data. The source, 8C 0821+695, was noted in the 8C survey data (Rees 1990) by Lacy et al. (1993), who measured the size of the source to be $1.5 \, h^{-1}$ Mpc and to have a redshift of 0.538. They estimate the age of the source to be $\sim 3 \times 10^7$ yr and argue that the source is large because it has expanded rapidly in a low-density environment rather than because it is old. Assuming no variability, the 10C data imply the spectral steepening of the emission from the central component; Lacy et al. (1993) found a spectral index for the central component of 0.23 ± 0.04 between 1.4 and 5 GHz. The 10C measurements imply a spectral index for the central component of 0.79 ± 0.06 between 5 and 15.7 GHz.

8 CONCLUSIONS

The AMI LA has been used to carry out the 10C survey, the deepest radio source survey of any significant extent ($\gtrsim 0.2$ deg^2) above 1.4 GHz. The resulting deep 15.7-GHz source counts are useful for the interpretation of CMB data, for which foreground radio sources are an important contaminant. The source catalogue also provides an invaluable resource for the study of faint high-frequency-selected radio sources. The survey covers ≈ 27 deg^2 complete to 1 mJy and ≈ 12 deg^2 (wholly contained within the larger area) complete to 0.5 mJy. The number of sources with $S > 25$ mJy, appearing in the survey catalogue, is biased low; several of the survey fields were chosen to minimize the number of such sources appearing within the survey areas. In total, 1897 sources appear in the 4.62σ catalogue; the faintest being ≈ 100 μJy. A number of the key conclusions from the work are listed below.

(1) The 10C differential source count was parametrized using a broken power law. This was found to provide a significantly better fit to the data than a simpler, single-power-law parametrization. The best-fitting broken power law is

$$n(S) \equiv \frac{\mathrm{d}N}{\mathrm{d}S} \approx \begin{cases} 24 \left(\frac{S}{\mathrm{Jy}}\right)^{-2.27} \ \mathrm{Jy}^{-1} \ \mathrm{sr}^{-1} \ \text{for } 2.8 \leq S \leq 25 \ \mathrm{mJy} \\\\ 376 \left(\frac{S}{\mathrm{Jy}}\right)^{-1.80} \ \mathrm{Jy}^{-1} \ \mathrm{sr}^{-1} \ \text{for } 0.5 \leq S < 2.8 \ \mathrm{mJy}. \end{cases}$$

(2) After having applied corrections to the individual source flux densities measured as part of the 9C survey to account for the small difference in frequencies between the 9C and 10C surveys, the 9C and 10C data were combined. The addition of the 9C data allowed the calculation of the best estimate of the 15.7-GHz differential source count by improving the source-count statistics for $5.5 \leq S < 25$ mJy and by providing data for a complete sample of sources with
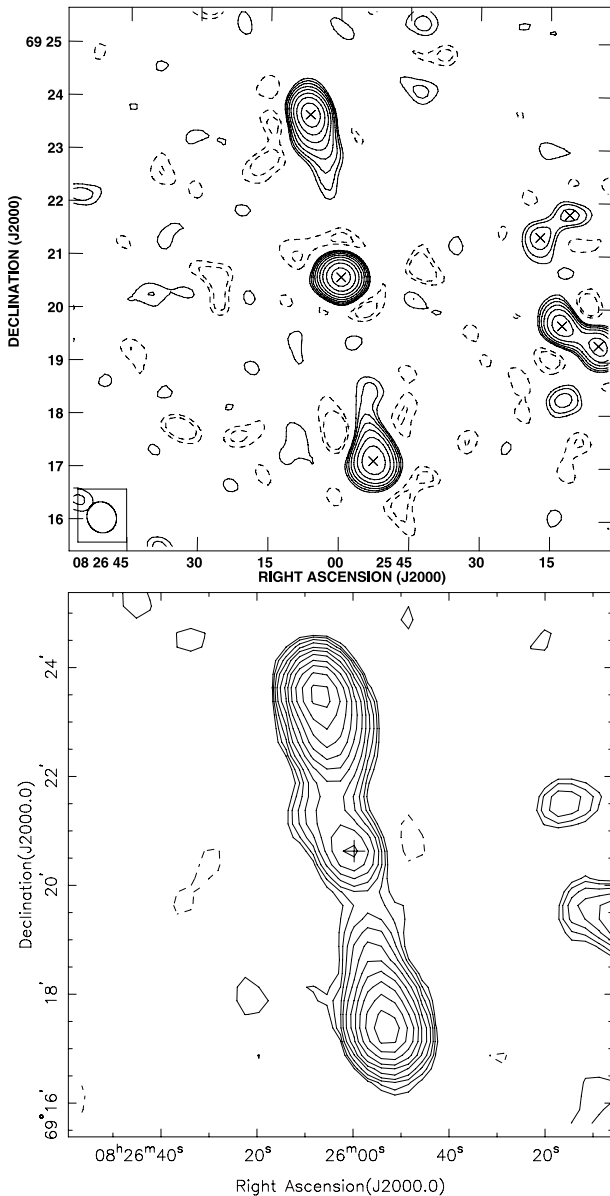
Figure 12. Contour plots of 8C 0821+695, a giant radio galaxy lying in one of the 10C survey fields, from the 10C survey at 15.7 GHz (top panel) and the NVSS at 1.4 GHz. In both cases, a factor of $\sqrt{2}$ separates the contours, which start at ± 0.1 and ± 1.0 mJy beam^{-1} for the 10C and NVSS plots, respectively. The negative contours are shown using the dashed lines. The crosses in the 10C plot indicate the position of 10C sources. The cross in the NVSS plot gives the position of the central component source at 15.7 GHz.

25 mJy $\leq S \leq 1$ Jy. Again, a broken-power-law parametrization was found to offer a significantly improved fit to the data compared with that provided by a single power law. The best-fitting broken power law is

$$n(S) \equiv \frac{\mathrm{d}N}{\mathrm{d}S} \approx \begin{cases} 48 \left(\frac{S}{\mathrm{Jy}}\right)^{-2.13} & \mathrm{Jy}^{-1}\ \mathrm{sr}^{-1} \text{ for } 2.2 \text{ mJy} \leq S \leq 1 \text{ Jy} \\ \\ 340 \left(\frac{S}{\mathrm{Jy}}\right)^{-1.81} & \mathrm{Jy}^{-1}\ \mathrm{sr}^{-1} \text{ for } 0.5 \leq S < 2.2 \text{ mJy.} \end{cases}$$

(3) The model counts by de Zotti et al. (2005) are found to demonstrate good agreement with the 9C and 10C data at the high-flux-density end of the measured count. However, with decreasing flux density the model first overpredicts and then, below about

5 mJy, underpredicts the measured count. By integrating the model differential source count, the model was found to underpredict the total number of sources, with flux densities between 0.5 mJy and 1 Jy, per unit area by approximately 30 per cent. This deficit, over the entire flux-density range, is attributable to the model underestimating the count at the lowest flux densities.

(4) Entries from the 10C source catalogue were matched to those contained in the catalogues of the NVSS and FIRST survey (both of which have observing frequencies of 1.4 GHz). The matching revealed a shift in the typical 1.4- to 15.7-GHz spectral index of the 15.7-GHz-selected source population with decreasing flux density towards sub-mJy levels. When matching to the NVSS, 49 per cent of sources with $5.0 \leq S_{10C} < 25.0$ mJy were found to have $\alpha_{1.4}^{15.7} > 0.81$. However, for sources with $0.5 \leq S_{10C} < 0.6$ mJy, the corresponding figure is 18 per cent. The observed trend is in contrast to that measured for sources with higher flux densities by Waldram et al. (2010). They found that the typical spectral index became steeper for sources with decreasing flux densities between ≈ 100 and ≈ 10 mJy. A similar effect, to that measured using the 10C data, has been observed as part of lower frequency surveys – in lower-frequency-selected samples, significant numbers of flatter spectrum sources start to enter at sub-mJy levels (see e.g. Prandoni et al. 2006, and references therein).

(5) Automated techniques for identifying extended sources, described in Paper I, have been applied to the data. The proportion of sources that are extended relative to the LA-synthesized beam of ≈ 30 arcsec is ≈ 5 per cent; this is similar to the proportion of ≈ 6 per cent measured by Waldram et al. (2003). A subset of 39 extended or overlapping sources, thought likely to be genuinely extended on the basis of their 15.7-GHz morphologies, were investigated further using higher resolution data. These data confirmed that at least 29 of these sources are genuinely extended; most were identified as classical doubles but three are nearby galaxies and four are twin-jet sources.

REFERENCES

AMI Consortium: Davies M. L. et al., 2009, MNRAS, 400, 984
AMI Consortium: Franzen T. M. O. et al., 2009, MNRAS, 400, 995
AMI Consortium: Franzen T. M. O. et al., 2011, MNRAS, in press, doi:10.1111/j.1365-2966.2011.18887.x (arXiv:1012.3711) (Paper I)
AMI Consortium: Zwart J. T. L. et al., 2008, MNRAS, 391, 1545
Becker R. H., White R. L., Helfand D. J., 1995, ApJ, 450, 559
Bolton R. C. et al., 2004, MNRAS, 354, 485
Bolton R. C., Chandler C. J., Cotter G., Pearson T. J., Pooley G. G., Readhead A. C. S., Riley J. M., Waldram E. M., 2006, MNRAS, 367, 323
Browne I. W. A., Wilkinson P. N., Patnaik A. R., Wrobel J. M., 1998, MNRAS, 293, 257
Condon J. J., Cotton W. D., Greisen E. W., Yin Q. F., Perley R. A., Taylor G. B., Broderick J. J., 1998, AJ, 115, 1693

de Zotti G., Gruppioni C., Ciliegi P., Burigana C., Danese L., 1999, New Astron., 4, 481

de Zotti G., Ricci R., Mesa D., Silva L., Mazzotta P., Toffolatti L., González-Nuevo J., 2005, A&A, 431, 893

Eddington A. S., 1913, MNRAS, 73, 359

Holler C. M., Kaneko T., Jones M. E., Grainge K., Scott P., 2007, A&A, 464, 795

Lacy M., Rawlings S., Saunders R., Warner P. J., 1993, MNRAS, 264, 721

López-Caniego M., González-Nuevo J., Herranz D., Massardi M., Sanz J. L., De Zotti G., Toffolatti L., Argüeso F., 2007, ApJS, 170, 108

Massardi M. et al., 2008, MNRAS, 384, 775

Massardi M. et al., 2011, MNRAS, 412, 318

Murphy T. et al., 2010, MNRAS, 402, 2403

O'Dea C. P., 1998, PASP, 110, 493

Patnaik A. R., Browne I. W. A., Wilkinson P. N., Wrobel J. M., 1992, MNRAS, 254, 655

Prandoni I., Parma P., Wieringa M. H., de Ruiter H. R., Gregorini L., Mignano A., Vettolani G., Ekers R. D., 2006, A&A, 457, 517

Rees N., 1990, MNRAS, 244, 233

Ricci R. et al., 2004, MNRAS, 354, 305

Sadler E. M. et al., 2006, MNRAS, 371, 898

Tauber J. A. et al., 2010, A&A, 520, 1

Taylor A. C., Grainge K., Jones M. E., Pooley G. G., Saunders R. D. E., Waldram E. M., 2001, MNRAS, 327, L1

Waldram E. M., Pooley G. G., Grainge K. J. B., Jones M. E., Saunders R. D. E., Scott P. F., Taylor A. C., 2003, MNRAS, 342, 915

Waldram E. M., Pooley G. G., Davies M. L., Grainge K. J. B., Scott P. F., 2010, MNRAS, 404, 1005

Wilkinson P. N., Browne I. W. A., Patnaik A. R., Wrobel J. M., Sorathia B. 1998, MNRAS, 300, 790

APPENDIX A: MODEL SOURCE COUNTS

Table A1 shows the 15-GHz model source counts by de Zotti et al. (2005) with which the measured 9C and 10C source counts are compared in Section 5.2. Here, the model counts are provided only for the flux-density range relevant for comparison to 9C and 10C data.

SUPPORTING INFORMATION

Additional Supporting Information may be found in the online version of this article:

Table 1. The 10C source list of 1897 sources.

Table A1. 15-GHz model source counts by de Zotti et al. (2005), presented as logarithmic, normalized differential counts – specifically $\log_{10}(S^{5/2} \mathrm{d}N/\mathrm{d}S)$. Predicted counts are given for a number of different source populations; the flat-spectrum counts are made up of the sum of the flat-spectrum-radio-quasar (FSRQ) and BL-Lacertae (BL Lac) counts, and the total counts are found by summing the flat-spectrum and steep-spectrum counts.

$\log_{10} S$ (Jy)	Source count (Jy$^{1.5}$ sr^{-1})				
	FSRQ	BL Lac	Flat spectrum	Steep spectrum	Total
−4.000	−1.563	−1.020	−0.911	−1.084	−0.688
−3.900	−1.479	−0.972	−0.854	−0.935	−0.592
−3.800	−1.395	−0.924	−0.797	−0.778	−0.487
−3.700	−1.311	−0.876	−0.740	−0.609	−0.369
−3.600	−1.226	−0.829	−0.682	−0.445	−0.247
−3.500	−1.142	−0.781	−0.624	−0.319	−0.144
−3.400	−1.058	−0.735	−0.566	−0.215	−0.055
−3.300	−0.974	−0.688	−0.507	−0.119	0.030
−3.200	−0.890	−0.642	−0.447	−0.028	0.112
−3.100	−0.806	−0.596	−0.387	0.059	0.192
−3.000	−0.721	−0.550	−0.326	0.146	0.272
−2.900	−0.637	−0.505	−0.265	0.232	0.352
−2.800	−0.553	−0.460	−0.203	0.316	0.431
−2.700	−0.469	−0.415	−0.140	0.400	0.510
−2.600	−0.385	−0.371	−0.077	0.483	0.588
−2.500	−0.301	−0.327	−0.013	0.564	0.666
−2.400	−0.217	−0.283	0.052	0.643	0.742
−2.300	−0.133	−0.240	0.118	0.721	0.818
−2.200	−0.050	−0.197	0.184	0.795	0.890
−2.100	0.034	−0.155	0.251	0.868	0.962
−2.000	0.118	−0.113	0.319	0.935	1.029
−1.900	0.201	−0.071	0.387	0.998	1.093
−1.800	0.285	−0.029	0.456	1.056	1.153
−1.700	0.368	0.012	0.526	1.103	1.205
−1.600	0.451	0.052	0.597	1.140	1.249
−1.500	0.534	0.092	0.668	1.163	1.284
−1.400	0.616	0.132	0.739	1.163	1.302
−1.300	0.698	0.172	0.811	1.137	1.305
−1.200	0.779	0.211	0.883	1.103	1.308
−1.100	0.860	0.250	0.955	1.076	1.321
−1.000	0.939	0.288	1.027	1.052	1.340
−0.900	1.018	0.326	1.098	1.028	1.366
−0.800	1.095	0.363	1.169	1.003	1.395
−0.700	1.170	0.401	1.238	0.977	1.428
−0.600	1.242	0.438	1.305	0.951	1.464
−0.500	1.310	0.474	1.369	0.924	1.502
−0.400	1.373	0.510	1.429	0.898	1.541
−0.300	1.430	0.546	1.483	0.873	1.579
−0.200	1.479	0.581	1.531	0.850	1.613
−0.100	1.517	0.616	1.568	0.827	1.641
0.000	1.543	0.651	1.595	0.805	1.660

This paper has been typeset from a TeX/LaTeX file prepared by the author.